ISSN 1063-7834, Physics of the Solid State, 2018, Vol. 60, No. 9, pp. 1752–1761. © Pleiades Publishing, Ltd., 2018.
Original Russian Text © A.S. Kamzin, H. Das, N. Wakiya, A.A. Valiullin, 2018, published in Fizika Tverdogo Tela, 2018, Vol. 60, No. 9, pp. 1707–1716.

MAGNETISM

Magnetic Core/Shell Nanocomposites $MgFe_2O_4/SiO_2$ for Biomedical Application: Synthesis and Properties

A. S. Kamzin[a, *], H. Das[b, c], N. Wakiya[d, e], and A. A. Valiullin[f]

[a] *Ioffe Institute, St. Petersburg, 194021 Russia*
[b] *Graduate School of Science and Technology, Shizuoka University, 3-5-1 Johoku, Naka-ku, Hamamatsu 432-8561, Japan*
[c] *Materials Science Division, Atomic Energy Centre, Dhaka 1000, Bangladesh*
[d] *Department of Electronics and Materials Science, Shizuoka University, 3-5-1 Johoku, Naka-ku, Hamamatsu 432-8561, Japan*
[e] *Research Institute of Electronics, Shizuoka University, 3-5-1 Johoku, Naka-ku, Hamamatsu 432-8561, Japan*
[f] *Kazan Federal University, Kazan, Tatarstan, 420008 Russia*
** e-mail: Kamzin@mail.ioffe.ru*

Received January 23, 2018; in final form, March 15, 2018

Abstract—Magnetic core/shell (CS) nanocomposites (MNCs) are synthesized using a simple method, in which a magnesium ferrite nanoparticle ($MgFe_2O_4$) is a core, and an amorphous silicon dioxide (silica SiO_2) layer is a shell. The composition, morphology, and structure of synthesized particles are studied using X-ray diffraction, field emission electron microscopy, transmission electron microscopy (TEM), energy-dispersive spectroscopy (EDS), scattering electrophoretic photometer, thermogravimetric analysis (TGA), and Mössbauer spectroscopy. It is found that the $MgFe_2O_4/SiO_2$ MNC has the core/shell structure formed by the Fe–O–Si chemical bond. After coating with silica, the $MgFe_2O_4/SiO_2$ MNC saturation magnetization significantly decreases in comparison with $MgFe_2O_4$ particles without a SiO_2 shell. Spherical particles agglomerated from $MgFe_2O_4$ nanocrystallites ~9.6 and ~11.5 nm in size function as cores coated with SiO_2 shells ~30 and ~50 nm thick, respectively. The total size of obtained CS MNCs is ~200 and 300 nm, respectively. Synthesized CS $MgFe_2O_4/SiO_2$ MNCs are very promising for biomedical applications, due to the biological compatibility of silicon dioxide, its sizes, and the fact that the Curie temperature is in the region required for hyperthermal therapy, 320 K.

DOI: 10.1134/S1063783418090147

1. INTRODUCTION

Due to their unique magnetic properties, magnetic nanoparticles (MNPc) of magnesium ferrite spinel ($MgFe_2O_4$) are promising for a wide spectrum of applications in biomedical fields, such as a contrasting agent in magnetic resonance tomography, carriers for targeted drug delivery, heat sources in hyperthermal therapy, and biochemical sensing [1–4]. It was shown that the ferrite–spinel $MgFe_2O_4$ MNPs have a higher heatability under an external ac magnetic field, than other ferrite–spinels, and, hence, are the most efficient MNPs for magnetic hyperthermal therapy of human malignant tumors [5–10]. Furthermmore, ferrite $MgFe_2O_4$ consists of elements being nontoxic and biologically compatible for a living organism [10].

$MgFe_2O_4$ MNPs were synthesized using various methods, i.e., coprecipitation, sol–gel, mechanochemical, burning, and microwave hydrothermal synthesis and polymerization (see [10–12] and references therein). However, there are difficulties in $MgFe_2O_4$ MNP synthesis, e.g., at the synthesis stage or after MNP annealing, grains of sintered particles can be formed in air [13, 14], which prevents the uses of such particles in biomedicine. One of the efficient methods for producing $MgFe_2O_4$ MNPs is ultrasonic aerosol pyrolysis (UAP), which allows for obtaining dried spherical nanoparticles in the superparamagnetic state with controlled composition, high purity, good crystallinity, and morphology for a rather short time [10–13, 15].

The specificity of $MgFe_2O_4$ MNP biomedical applications is significantly restricted due to the poor dispersibility of these particles in aqueous solutions, and the tendency to agglomeration and oxidation with possible decomposition caused by an ambient medium [16–18]. The development of core/shell magnetic nanocomposites (MNPs) in which the non-

magnetic shell coats the magnetic nanoparticles surface offers new opportunities for preventing the above restriction and increasing the particle efficiency [19]. The MNP shell can be biologically compatible organic surfactants, gold, silica SiO_2, polymers, and others. Among the above materials, silica is the best one as a shell, since it is nontoxic, easily dispersed in water, thermostable, and has a high biocompatibility [16, 19, 20]. The SiO_2 shell also provides a chemically inert surface protecting nanoparticles from leaching in an acidic medium. The silica surface contains silane groups allowing conjugation of its surface with various functional materials and the formation of covalent bonds –Si–O–Si– in biological systems [21]. MNPs were coated with silicon dioxide using various methods, i.e., microemulsion [16], sol–gel [18], and Stöber methods [21]. Increasingly widespread is the method for coating MNPs with a silica layer by the sol–gel method, which has a number of advantages, e.g., systematic monitoring of reaction parameters, and growth of high-purity and homogeneous layers of controllable thickness [18, 22–24]. Furthermore, chemical substances harmless to an ambient medium, such as water, ethanol, and silicon dioxide, are used in the sol–gel method.

There are a number of publications and developments of the sol–gel method, e.g., by studying the effect of various parameters, such as the temperature, precursor composition, catalyst type, and others [22, 25, 26]. The amorphous SiO_2 layer was mostly grown by hydrolysis and condensation of alkoxysilanes such as tetraethyl orthosilicate (TEOS) with an added acidic or basic catalyst. Physical and chemical properties of synthesized MNPs depend to a large extent on the catalyst type used in the reaction.

The objective of this study was (i) to synthesize CS ($MgFe_2O_4/SiO_2$) magnetic nanocomposites (MNCs) in which cores are ferrite–magnesium ($MgFe_2O_4$) MNPs and shells are amorphous layers of silicon dioxide (or silica SiO_2); (ii) to select a catalyst promoting the formation of a homogeneous amorphous SiO_2 layer on the $MgFe_2O_4$ MNP surface without changing the MNP microstructure; and (iii) to perform systematic studies of obtained $MgFe_2O_4$ MNPs and core/shell $MgFe_2O_4/SiO_2$ MNCs to determine the CS MNP synthesis technology and to understand the effect of the SiO_2 shell on structural and magnetic properties of $MgFe_2O_4$ MNPs being cores.

2. SYNTHESIS OF MAGNETIC $MgFe_2O_4$ NANOPARTICLES AND $MgFe_2O_4/SiO_2$ NANOCOMPOSITES

CS $MgFe_2O_4/SiO_2$ MNCs were synthesized in two stages: the first stage is $MgFe_2O_4$ MNP synthesis by the ultrasonic aerosol pyrolysis method; the second stage is the development of core/shell MNPs by applying a SiO_2 shell by the sol–gel method on $MgFe_2O_4$ MNPs. $MgFe_2O_4$ MNPs were synthesized using 99% pure grade materials with high solubility in water, i.e., magnesium nitrate hexahydrate ($Mg(NO_3)_2 \cdot 6H_2O$) and iron (III) nitrate nonahydrate ($Fe(NO_3)_3 \cdot 9H_2O$). SiO_2 shell was applied using tetraethyl orthosilicate (TEOS, 99.9%); 1-M hydrochloric acid (HCl, 99.9%) was used as a catalyst. Deionized water was used as a solvent.

In the first stage, $MgFe_2O_4$ nanoparticles were synthesized from magnesium and iron nitrate solutions in distilled water in the molar ratio Mg : Fe = 1 : 2 in concentrations 0.06 and 0.12 M, respectively, as it was described in [11]. Precursors for synthesizing $MgFe_2O_4$ nanoparticles of different sizes by the ultrasonic aerosol pyrolysis (UAP) method were prepared by mixing these solutions. In the UAP method, the precursor is sprayed using an ultrasonic vibrator at the resonant frequency of 1.6 MHz, and the obtained drops are transferred by a gas flow to a tube-shaped quartz reactor mounted in an electric furnace (ARF-50KC, Kobe, Japan). Drops are evaporated in the reactor, decay, and/or crystallize into ferrite–spinel particles [10, 11, 15]. During pyrolysis, a temperature of 700°C was maintained in the furnace, since MNPs with good crystallinity and morphology were obtained at this temperature [11, 15]. As a result, as studies showed, $MgFe_2O_4$ nanocrystallites ~9.6 and ~11.5 nm in size were synthesized from precursors of 0.06 and 0.12 M, respectively, which are agglomerated into spherical particles from ~200 to ~300 nm in diameter.

In the second stage, silicon dioxide (SiO_2) shells were applied on $MgFe_2O_4$ particles synthesized by the sol–gel method. To this end, $MgFe_2O_4$ particles were dispersed into deionized water and were deglamorized in an ultrasonic cleaning bath for 1 h. A solution consisting of deionized water (10 mL), TEOS (330 mL), and catalyst HCl (14.5 mL) was added into the obtained suspension, and the mixture was continuously stirred for 12 h at a temperature of 70°C.

To provide complete MNP coverage by silicon dioxide, the obtained suspension was ultrasonicated for 24 h. After that, the precipitate was separated from the solution using a centrifuge and, to minimize particle agglomeration, was sprayed into ethanol. This rinsing process was repeated three times. Then the precipitate was removed and dried at 80°C for 5 h. As a result, as studies showed, CS spherical $MgFe_2O_4/SiO_2$ nanoparticles were synthesized.

3. EXPERIMENTAL TECHNIQUE

X-ray diffraction patterns (XRDPs) of powder samples of synthesized $MgFe_2O_4$ MNPs and $MgFe_2O_4/SiO_2$ MNCs were measured using an X-ray diffractometer (D8 Advance, Broker Analytik, Germany) with Cu$K\alpha_1$ radiation ($\lambda = 1.5418$ Å), at a volt-

age of 40 kV and a current of 40 mA, in the 2θ mode with a scanning rate of 0.01 s^{-1}. The particle phase composition was analyzed using the TOPAS software with the ICSD PDF database [27]. The MNC shell morphology was studied using a field emission scanning electron microscope (FESEM) (JSM-700F, JEOL Ltd., Tokyo, Japan) with an accelerating voltage of 15 kW and a scanning transmission electron microscope (STEM) (JEM-2100F, JEOL Ltd.) with an accelerating voltage of 200 kW. The chemical composition was analyzed using an energy-dispersive X-ray spectrometer (EDXS) incorporated into the TEM. The particle size distribution was measured using a scattering electrophoretic photometer (Photal SELS-800Y, Otsuka Electronics Co. Ltd. Tokyo, Japan). For these measurements, a powder was dispersed into ethanol and was ultrasonicated for 10 min; one drop was precipitated on a grid coated with carbon, and was dried overnight before the STEM analysis. Samples of $MgFe_2O_4$ MNPs without shell and CS $MgFe_2O_4/SiO_2$ MNC were studied using a differential thermal and thermogravimetric analyzer (DT-TGA) with a Thermoplus TG 8120 spectrometer (Rigaku, Japan) in air with an Al_2O_3 reference container. Measurements were performed in a temperature range of 25–1000°C; the heating rate was 10°C/min.

The magnetic parameters were measured at room temperature using a vibrating sample magnetometer (VSM) (BHV-35; Riken Denshi Co. Ltd. Tokyo, Japan) with a maximum magnetic field of 10 kOe. The magnetization was calibrated by the standard sample of Ni foil. The temperature dependences of magnetic parameters were obtained in a magnetic field strength to 100 Oe in the temperature range of from room temperature to 400°C. All measurements were performed at identical sweep rates and step sizes.

One of the most important problems in studying synthesized nanoparticles is the phase and magnetic state identification. To these ends, Mössbauer spectroscopy is very efficient. The hyperfine interaction parameters obtained from Mössbauer spectra (MSs) for various ferrite–shpinels or magnetic states differ significantly, which makes it possible to solve the important problem of the phase analysis, magnetic structure, and magnetic states of materials using Mössbauer spectroscopy. Therefore, to study synthesized particles, ^{57}Fe Mössbauer spectroscopy with γ-ray recording in transmission mode was used. The reference signal in the motion system of the Doppler modulator in the spectrometer was triangle-shaped to set the Co^{57}(Rd) gamma-ray source velocity with constant acceleration. The velocity scale was calibrated at room temperature using an alpha-iron foil 6 μm thick; more accurate calibration was performed using a laser interferometer.

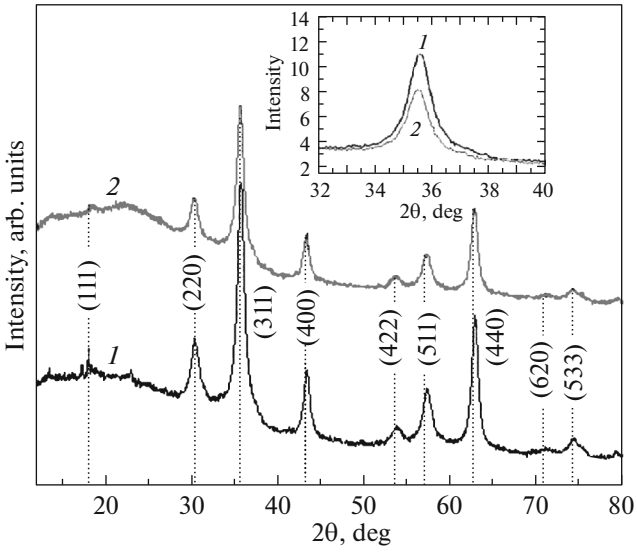

Fig. 1. X-ray diffraction patterns of powder samples: (*1*) $MgFe_2O_4$ nanoparticles and (*2*) core/shell $MgFe_2O_4/SiO_2$ nanocomposites. The inset shows the (311) X-ray diffraction line intensities for (*1*) $MgFe_2O_4$ nanoparticles and (*2*) $MgFe_2O_4/SiO_2$ nanocomposites.

MSs of studied $MgFe_2O_4$ MNPs were measured at room temperature. The mathematical treatment of experimental MSs was performed using the program [28].

The divergences of the theoretical parameter of hyperfine interactions are determined from statistical deviations presented by the mathematical treatment program [28].

4. EXPERIMENTAL RESULTS AND DISCUSSION

4.1. X-Ray Diffraction Data

Figure 1 shows the X-ray diffraction patterns (XRDPs) of synthesized $MgFe_2O_4$ MNPs without shell and CS $MgFe_2O_4/SiO_2$ MNCs. The lines obtained for $MgFe_2O_4$ MNPs and MNC $MgFe_2O_4/SiO_2$ MNCs are in agreement with to the positions of XRDP database lines for $MgFe_2O_4$ (ICSD no. 01-0171-1232), pointing to the high phase homogeneity of obtained magnetic particles. The XRDP lines are sufficiently wide, which indicates the nanocrystalline nature of formed particles, and the sharpness (clearness) of lines indicates the high degree of crystallization. Using the TOPAS software, it was found that the average size of $MgFe_2O_4$ nanomonocrystallites is ~9.6 and ~11.5 nm, which is consistent with the data of [11, 15]. The absence of distinct lines attributed to SiO_2 of $MgFe_2O_4/SiO_2$ MNCs in XRDP is caused by the shell structure amorphicity and the absence of crystallization. However, the broad

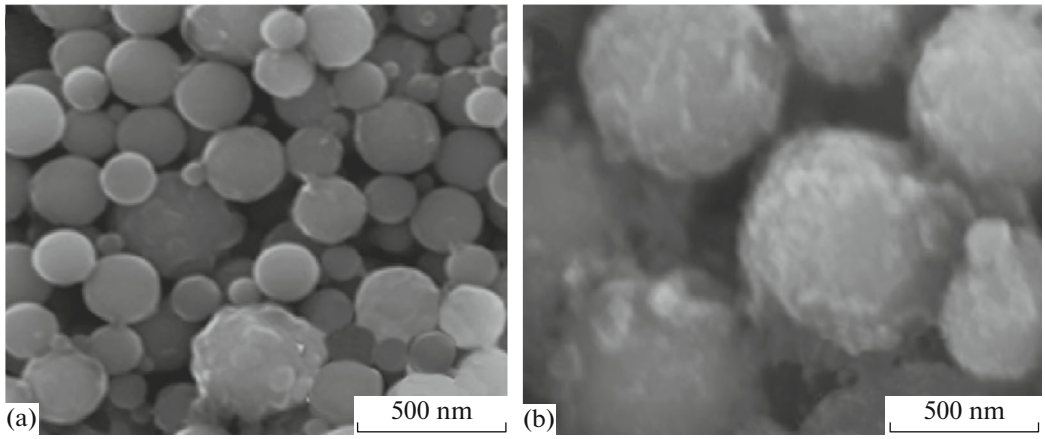

Fig. 2. FESEM micrographs of powder samples: (a) $MgFe_2O_4$ nanoparticles and (b) core/shell $MgFe_2O_4/SiO_2$ nanocomposites.

line observed in the $MgFe_2O_4/SiO_2$ MNC XRDP in the range between 20° and 25° indicates the silicon dioxide presence on the MNC surface, which is consistent with the data of [18]. For comparison, the inset in Fig. 1 shows the (311) X-ray lines for MNPs and MNCs; we can see that lines are identical in width at half height of peaks; however, in the case of $MgFe_2O_4/SiO_2$ MNCs, the line intensity is lower than for $MgFe_2O_4$ MNPs without a shell. This is probably due to the presence of a silica layer on the $MgFe_2O_4/SiO_2$ MNC. A similar pattern was observed on the magnetite MNP in silicon [29]. The data obtained allow the conclusion that there is a silica layer on the $MgFe_2O_4/SiO_2$ MNC surface, which does not change the $MgFe_2O_4$ MNP crystal structure.

4.2. $MgFe_2O_4$ Nanoparticle and $MgFe_2O_4/SiO_2$ Nanocomposite Morphology

Morphological features of MNPs and MNCs were analyzed by FESEM micrographs shown in Figs. 2a and 2b, respectively. We can see in Fig. 2a that the $MgFe_2O_4$ MNP has a smooth surface and a regular spherical shape without any cavities, grooves, or asymmetry. The average $MgFe_2O_4$ MNP diameter is larger than the size calculated based on the XRD data. Hence, it can be concluded that the $MgFe_2O_4$ MNCs are associated (agglomerated) into nanoclusters as was described in [11, 15] for $MgFe_2O_4$ nanoparticles from [14] for barium hexaferrite particles. Figure 2b shows that $MgFe_2O_4$ MNPs in SiO_2 shells retain spherical morphology, but the MNC surface becomes slightly rough. When comparing Figs. 2a and 2b, we can see that $MgFe_2O_4/SiO_2$ MNCs are significantly larger than $MgFe_2O_4$ particles, which also indicates the shell formation on the $MgFe_2O_4$ MNP surface. In Fig. 2b, we can see particle agglomeration regions.

The elemental composition of samples, determined using energy-dispersive X-ray analysis (EDRA), is shown in Table 1. An elemental analysis shows that $MgFe_2O_4$ MNPs contain only Mg, Fe, and O ions. The experimentally determined percentages of elements are close to theoretical values. Si ions in synthesized $MgFe_2O_4$ MNPs without shell are absent, although the presence of Si is possible due to a quartz tube used for UAP [30]. It is well known that the EDRA method allows the determination of the atom concentration in the crystal surface layers. After applying a silica shell on the $MgFe_2O_4$ MNP, one more line (see Table 1(b)) appears, attributed to Si ions, whose intensity is 11.74 at %. From this it follows that $MgFe_2O_4/SiO_2$ MNCs consist of two phases, i.e.,

Table 1. Elemental composition of (a) $MgFe_2O_4$ nanoparticles and (b) $MgFe_2O_4/SiO_2$ nanocomposites, determined from the energy-dispersive X-ray spectra (Wt is the weight percent, At is the atomic percent)

(a) Chem. element	Wt %	At %	(b) Chem. element	Wt %	At %
O	37.93	63.48	O	41.33	63.84
Mg	10.87	11.97	Mg	7.57	7.70
Fe	51.20	24.55	Si	13.38	11.78
Total	100.00	100.00	Fe	37.71	16.69
			Total	100.00	100.00

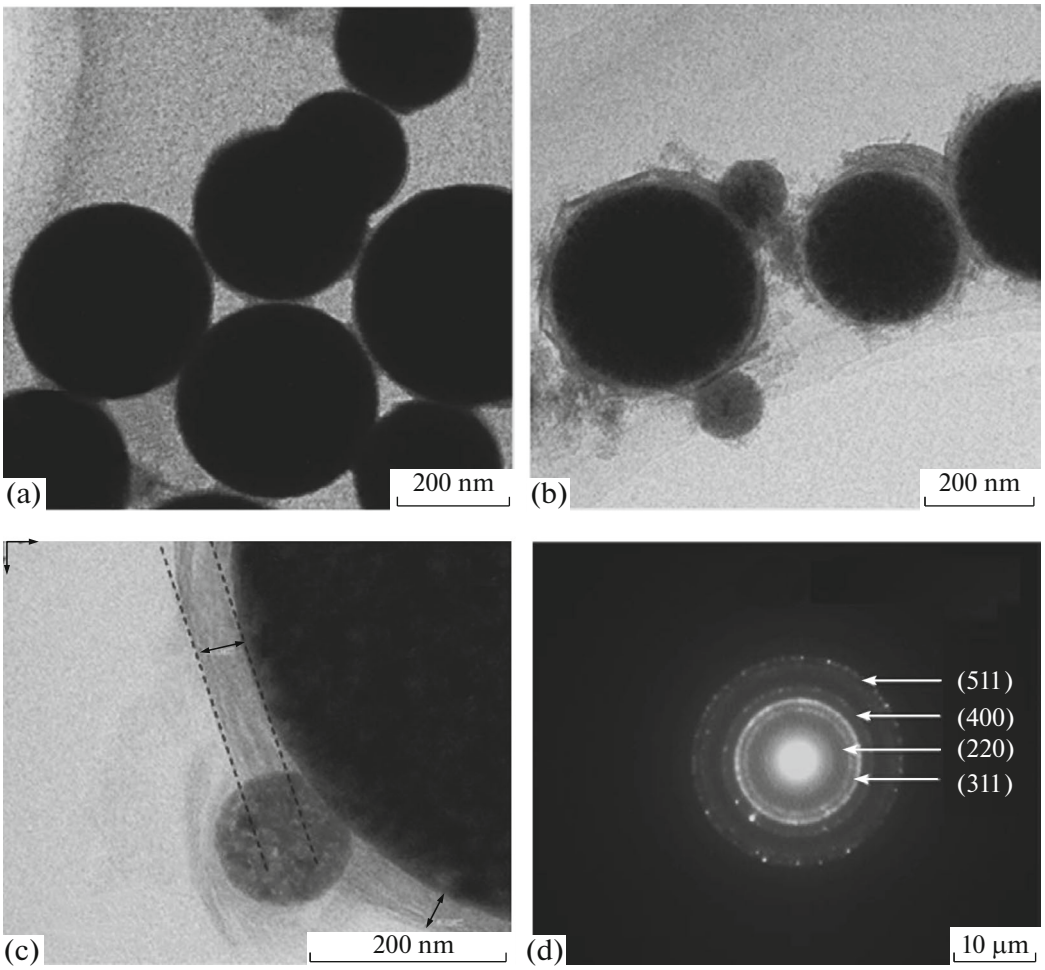

Fig. 3. Transmission-type micrographs obtained using a high-resolution electron microscope: (a) $MgFe_2O_4$ nanoparticles, (b and c) core/shell $MgFe_2O_4/SiO_2$ nanocomposites, (d) electron diffraction in a chosen $MgFe_2O_4/SiO_2$ nanocomposite area.

$MgFe_2O_4$ and SiO_2. No Cl or other ion impurities that can be formed during MNP coating with shell were observed, which is consistent with the data of [30]. A quantitative estimation of EDRA data for $MgFe_2O_4$ MNPs showed that the MNP composition close to the nominal one (I,U,W), i.e., 1 : 2 : 4.

4.3. Transmission Electron Microscopy (TEM) Data

Figures 3a–3c show the TEM micrographs of synthesized $MgFe_2O_4$ and $MgFe_2O_4/SiO_2$ particles. $MgFe_2O_4$ MNPs represent a magnetic material; therefore, the area of $MgFe_2O_4$ particles in Fig. 4a is dark with distinct undiffused boundaries. Silica (SiO_2) is a nonmagnetic oxide; therefore, this material is seen in TEM micrographs as a bright area. After applying silica shells on $MgFe_2O_4$ MNPs, as seen in Fig. 3b, a bright halo formed by a relative homogeneous amorphous SiO_2 layer is observed around magnesium ferrite particles. A similar pattern was observed in the case of the core/shell $SrFe_{12}O_{19}/SiO_2$ MNC [31]. Hence, the $MgFe_2O_4/SiO_2$ MNC consists of two phases, i.e., $MgFe_2O_4$ and SiO_2. We can see in the high-magnification TEM micrograph (Fig. 4c) that the SiO_2 shell tightly contacts with the $MgFe_2O_4$ particle and forms the CS structure with pronounced boundary layer. The thicknesses of SiO_2 shells coating particles of agglomerated nanomonocrystallites ~9.6 and ~11.5 nm in size are ~30 and ~50 nm, respectively. The $MgFe_2O_4/SiO_2$ MNC structure was studied in detail by the electron diffraction micrograph of a chosen sample area shown in Fig. 3d. The observed diffraction rings correspond to the spinel structure; rings indicating the presence of another phase are not observed. Based on the EDRA experimental data and HRTEM micrographs of $MgFe_2O_4$ MNPs and $MgFe_2O_4/SiO_2$ MNCs, it can be argued that $MgFe_2O_4$ particles are coated with a silicon dioxide layer, forming CS MNCs in which the MNP is the core and SiO_2 is the shell.

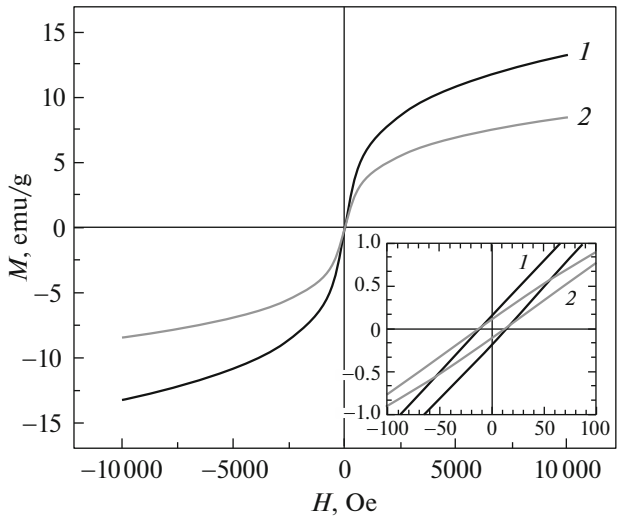

Fig. 4. Room-temperature hysteresis loops of (*1*) $MgFe_2O_4$ nanoparticles and (*2*) core/shell $MgFe_2O_4/SiO_2$ nanocomposites. The inset shows coercivity areas on an enlarged scale.

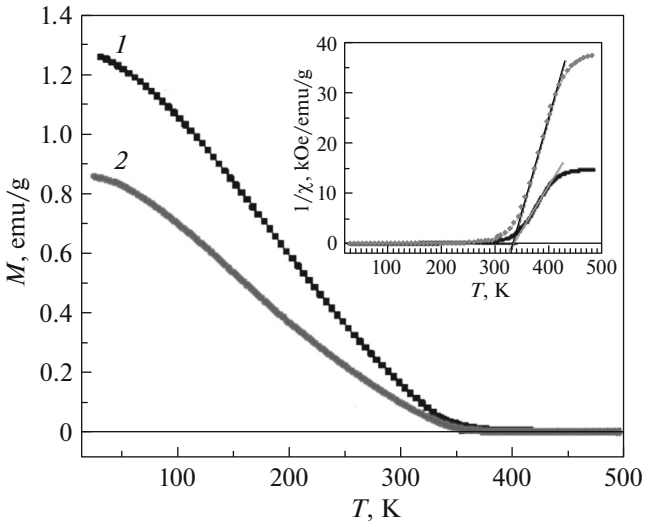

Fig. 5. Temperature dependences of the magnetization (*M*) of (*1*) $MgFe_2O_4$ nanoparticles and (*2*) core/shell $MgFe_2O_4/SiO_2$ nanocomposites, measured in the external magnetic field $H = 100$ Oe. The inset shows the inverse susceptibility ($1/\chi$) as a function of temperature with the indicated Curie temperatures ($T_C = 330$°C).

4.4. Magnetic Properties

The magnetic parameters of $MgFe_2O_4$ MNPs and $MgFe_2O_4/SiO_2$ MNCs were measured using MBO. Figure 4 shows the room-temperature dependences of the magnetization on an external magnetic field to ±10 kOe; the inset in Fig. 4 shows these dependences on an enlarged scale. The nonlinear shape of the hysteresis loop points to ferromagnetic ordering of $MgFe_2O_4$ MNPs; however, magnetization saturation is not observed even under a maximum possible magnetic field. It can be assumed that magnetic moment disordering on the $MgFe_2O_4$ MNP surface prevents magnetization saturation even at stronger external magnetic fields.

The saturation magnetization (Ms) of $MgFe_2O_4/SiO_2$ MNCs is 11 emu/g that is below Ms in $MgFe_2O_4$ MNPs (16.8 emu/g). Such disagreement of Ms probably reflects the effect of the amorphous nonmagnetic SiO_2 shell, leading to $MgFe_2O_4$ MNP magnetism shielding. Hence, the nonmagnetic layer of the SiO_2 shell can be considered as a magnetically dead layer on the $MgFe_2O_4$ particle surface, affecting the surface layer magnetization. The $MgFe_2O_4$ MNP coercivity after coating with SiO_2 shell remains unchanged, as is seen in the inset in Fig. 4. The hysteresis loops of $MgFe_2O_4$ MNPs and $MgFe_2O_4/SiO_2$ MNCs are almost completely reversible. This indicates the insignificance of the remanent magnetization and coercivity, hence, the feasibility of the superparamagnetic state of both $MgFe_2O_4$ MNPs and $MgFe_2O_4/SiO_2$ MNCs. The critical size is the size smaller which particles are in the superparamagnetic state. Experimental observations of the superparamagnetism phenomenon are possible if the relaxation time is shorter than the measurement time. In the magnetization measurements, the measurement time is usually longer than the relaxation time. Taking this into consideration, it can be argued that the critical diameter of $MgFe_2O_4$ MNPs is ~15 nm [32]. The $MgFe_2O_4$ nanomonocrystallite sizes using which CS $MgFe_2O_4/SiO_2$ MNCs were synthesized are in the range from 9.5 to 12 nm, which is below the upper limit for the superparamagnetic behavior.

When using MNPs for hyperthermal therapy, the requirement of nanoparticle heating turn off upon reaching 45°C is extremely important. In MNPs whose Curie temperature (T_C) is ~318 K, the heating process under an external magnetic field (MF) is automatically turned off upon reaching ~45°C. This is the most important advantage of MNPs in applications for hyperthermal treatment [22].

As seen in Fig. 5, the magnetization (M) decreases with increasing particle temperature and approaches zero. The values of T_C determined from the temperature dependence of the inverse susceptibility ($1/\chi$) according to the Curie–Weiss law, as shown in the inset of Fig. 5 for $MgFe_2O_4$ MNPs and $MgFe_2O_4/SiO_2$ MNCs are identical and are ~320 K.

4.5. Mössbauer Studies of $MgFe_2O_4$ MNPs and $MgFe_2O_4/SiO_2$ MNCs

For Mössbauer measurements, $MgFe_2O_4$ MNP and $MgFe_2O_4/SiO_2$ MNC powders were placed into a

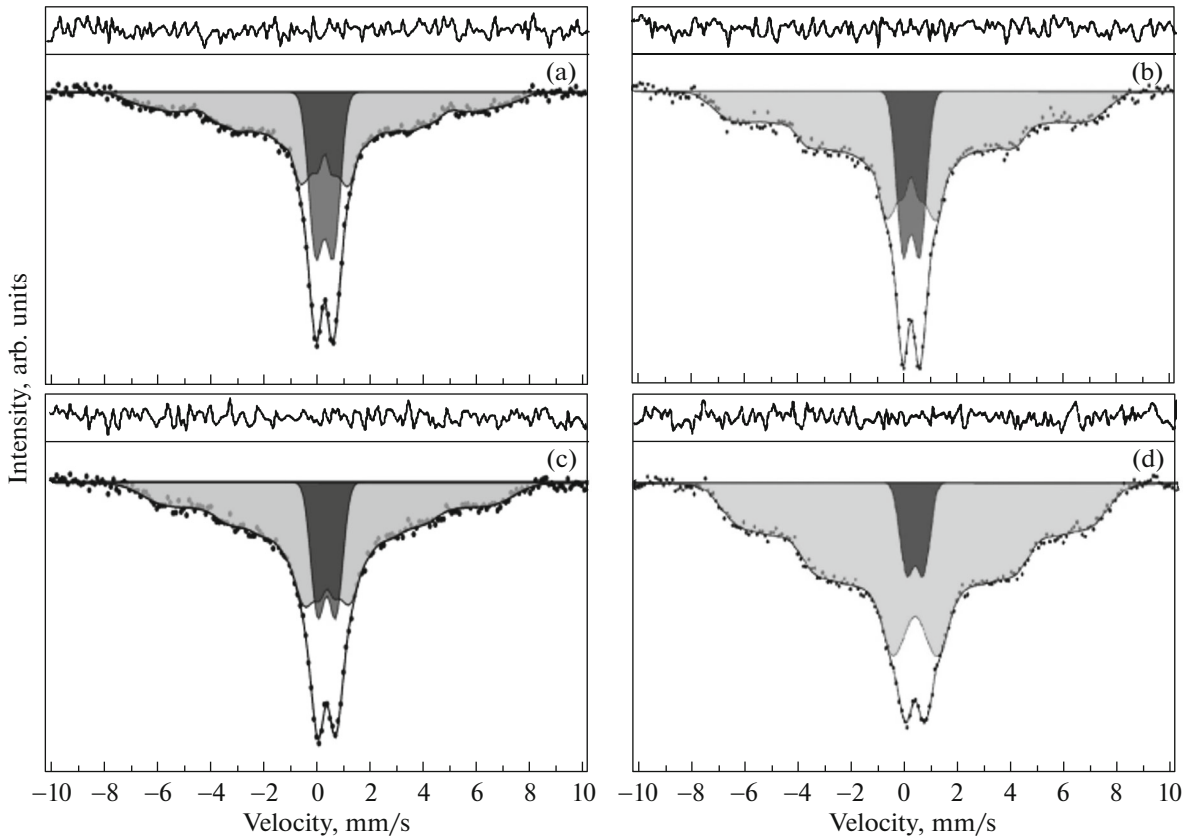

Fig. 6. Room-temperature Mössbauer spectra of (a, c) nanoparticles formed by agglomeration of $MgFe_2O_4$ nanocrystallites ~9.6 nm and ~11.5 nm in size and (b, d) core/shell $MgFe_2O_4/SiO_2$ MNCs synthesized based on $MgFe_2O_4$ particles, respectively. Dots are experimental values; model spectra obtained by processing using the SpectrRelax program are shaded. The differences between experimental data and model spectra are shown over each spectrum.

special evacuated plastic container kept without air access. Examples of room-temperature measurements of Mössbauer spectra (MS) of MNPs and MNCs are shown in Fig. 6. Room-temperature $MgFe_2O_4$ MNP and $MgFe_2O_4/SiO_2$ MNC MS (Fig. 6) have complex structures and consist of a doublet imposed on broadened Zeeman split lines. Such MS are characteristic of magnets in the SPM state (see, e.g., [33, 34], and references therein). The paramagnetic doublet can also be observed if the sample contains fine particles in which magnetic ordering is absent.

Mathematical treatment of experimental MS was performed using the SpectrRelax program [28] based on a multilevel relaxation model based on the quantum-mechanical description of a uniformly magnetized particle [34, 35]. The model spectra obtained using the SpectrRelax program [28] are shaded (Fig. 6), and experimental MS are displayed by dots. Over each spectrum in Fig. 6, the curves of disagreements of model spectra from experimental ones are shown, which indicate that experimental MS are quite satisfactory described by model ones. The hyperfine interaction parameters calculated from MS are shown in Table 2. As the MS processing results showed, MNPs and MNCs are characterized by a paramagnetic doublet with a low-intensity Zeeman sextet attributed to Fe^{3+} ions caused by the short relaxation times of spin moments.

If the observation time is much shorter than the relaxation time, the used experimental method allows observation of superparamagnetic phenomena. The relaxation time increases with the particle size. In Mössbauer spectroscopy, the observation time (τ) is $\sim 10^{-10}$ s [36]; therefore, MS of the disperse system of magnetic nanoparticles represents a superposition of the Zeeman sextet corresponding to large particles with the relaxation time of the magnetization vector longer than 10^{-8} s and the superparamagnetic doublet with broad lines corresponding to smaller particles with a relaxation time shorter than 10^{-8} s. At relaxation times shorter than 10^{-8} s, hyperfine magnetic splitting disappears and a paramagnetic doublet is observed. If the thermal energy is lower than the anisotropy energy barrier, the relaxation time is longer than the measurement time. In this case, magnetic moments of nanoparticles "freeze" along the easy magnetization axis, and Zeeman splitting lines appear in MS. Due to

Table 2. Effective magnetic fields (H_{eff}), isomeric chemical shifts (δ) with respect to α-Fe, quadrupole splits (Δ), linewidths (Γ), and line areas (RA)% for $MgFe_2O_4$ nanoparticles $M = 0.06$ and $M = 0.12$, 9.6, and 11.5 nm in size, respectively, and core/shell (CS) $MgFe_2O_4/SiO_2$ composites, calculated from room-temperature Mössbauer spectra

Sample	Fe	(H_{eff}) kOe	(Δ) mm/s	(δ) mm/s	(Γ) mm/s	(*RA*)%
$M = 0.06$	Doublet	–	0.34 ± 0.01	0.32 ± 0.01	0.62 ± 0.02	27 ± 6
9.6 nm	Sextet	77 ± 2	0.03 ± 0.02	0.35 ± 0.02	0.38 ± 0.13	73 ± 6
		270 ± 2				
$M = 0.12$	Doublet	–	0.33 ± 0.01	0.31 ± 0.01	0.62 ± 0.03	18 ± 2
11.5 nm	Sextet	79 ± 2	−0.03 ± 0.02	0.28 ± 0.02	0.23 ± 0.05	82 ± 2
		280 ± 2				
		360 ± 1				
CS 9.6	Doublet	–	0.32 ± 0.02	0.31 ± 0.01	0.59 ± 0.03	19 ± 2
	Sextet	88 ± 2	−0.01 ± 0.01	0.31 ± 0.02	0.71 ± 0.09	81 ± 2
		320 ± 2				
		395 ± 2				
CS 11.5	Doublet	–	0.32 ± 0.01	0.32 ± 0.01	0.60 ± 0.03	8 ± 2
	Sextet	98 ± 2	−0.02 ± 0.02	0.30 ± 0.02	0.29 ± 0.12	92 ± 2
		325 ± 2				
		410 ± 1				

the particle size distribution, a wide relaxation time distribution is observed in the sample, which leads to a set quasi-independent blocking processes and a corresponding blocking temperature distribution. The temperature below which the magnetization is stable, and particles behave as magnetically ordered crystals, is the blocking temperature [36].

The hyperfine interaction parameters obtained from experimental MS (Fig. 6) are given in Table 2. As seen in Table 2, the isomer shifts (δ) are from 0.31 to 0.35 mm/s, and quadrupole splittings (Δ) from 0.01 to 0.34 mm/s indicate that iron ions in $MgFe_2O_4$ MNPs and core/shell $MgFe_2O_4/SiO_2$ MNCs are in the high-spin Fe^{3+} state [36, 37]. The chemical shifts for iron ions in the low-spin state (Fe^{2+}) are from 0.9 to 1.1 mm/s [36, 38]; however, such values were not detected in processing experimental MS; hence, iron ions in the low-spin state (Fe^{2+}) are absent in the particles under study. The distribution function $P(H_{eff})$ for $MgFe_2O_4$-0.006 M MNPs can be described by three lines with maxima in the regions of 78, 270, and 350 kOe. In the case of $MgFe_2O_4$-0.12 M MNPs, these maxima in the distribution function $P(H_{eff})$ shift to the values of 82, 280, and 360 kOe (Fig. 7). In the $MgFe_2O_4$-0.06 M MNP MS, the paramagnetic doublet area is 27 ± 6%, whereas the Zeeman sextet area is 73 ± 6%. In the case of $MgFe_2O_4$-0.12 M MNPs, the paramagnetic doublet area decreases to 18 ± 2% in comparison with $MgFe_2O_4$-0.06 M MNPs, and the Zeeman sextet areas increases to 82 ± 2%. For $MgFe_2O_4/SiO_2$ MNCs obtained based on $MgFe_2O_4$ particles 9.6 and 11.5 nm in size, a decrease in the paramagnetic doublet area from 19 ± 2% to 8 ± 2%, respectively, is also observed, while the Zeeman sextet area increases from 81 ± 2% to 92 ± 2% (see Table 2). Such a decrease in the areas of paramagnetic lines, and an increase in the field peak positions in the $P(H_{eff})$ distribution curves clearly demonstrates that sizes of $MgFe_2O_4$ MNPs synthesized from precursors of 0.06 and 0.12 M, and CS $MgFe_2O_4/SiO_2$ MNCs obtained on their basis increase, but they retain the SPM state at room temperature.

According to calculations by the technique described in [39], spherical $MgFe_2O_4$ particles formed by $MgFe_2O_4$ nanocrystallite agglomeration are from 206 to 340 nm in size. However, this does not agree with Mössbauer data showing that the sizes of $MgFe_2O_4$ particles under study are ~10 nm, which allow superparamagnetic behavior. Based on the Mössbauer spectroscopy data, it can be argued that agglomeration of crystallites 9–11 nm in diameter into spherical particles 206–340 nm in size does not lead to the interaction of nanocrystallites with each other within these spheres, and MNPs behave in these spheres as individual crystallites from ~9 to ~11 nm in size.

The paramagnetic transition temperature of the bulk $MgFe_2O_4$ sample is higher than 900°C [40]. Based on Mössbauer and magnetic experimental data presented in this paper, it can be argued that the Curie temperature of synthesized CS $MgFe_2O_4/SiO_2$ MNCs is in the region of 320 K, which corresponds to the requirement on magnetic particles used in magnetic hyperthermal therapy.

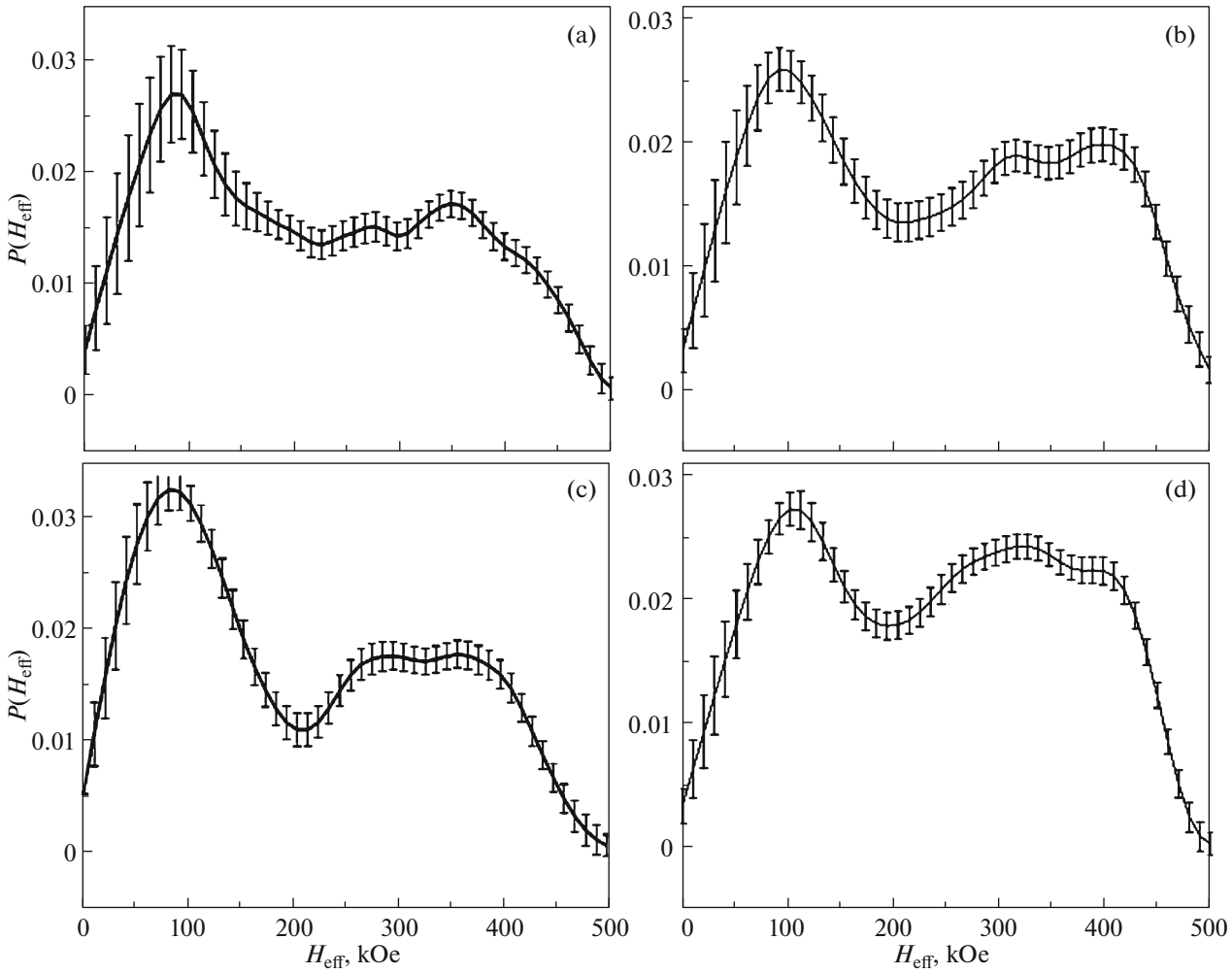

Fig. 7. Distributions of effective magnetic fields $P(H_{eff})$, reconstructed from experimental Mössbauer spectra: (a, c) nanoparticles formed by agglomeration of $MgFe_2O_4$ nanocrystallites ~9.6 and ~11.5 nm in size; (b, d) core/shell $MgFe_2O_4/SiO_2$ MNCs synthesized based on $MgFe_2O_4$ particles, respectively.

5. CONCLUSIONS

$MgFe_2O_4/SiO_2$ magnetic nanocomposites were synthesized by the two-stage method. It was found that obtained $MgFe_2O_4/SiO_2$ composites consist of spherical ferrite–shpinel $MgFe_2O_4$ particles forming a core coated with a silicon dioxide shell ~30–50 nm thick; thus, form core/shell (CS) MNCs. The sizes of CS MNCs are 200–300 nm. The SiO_2 shell was applied by hydrolysis and polycondensation of tetraethyl orthosilicate in an aqueous solution with added acid catalyst (HCl) playing an important role in the formation of the amorphous SiO_2 shell and preventing the formation of silica particles. Homogeneous dense shell layers were formed due to the effect of acid catalyst not changing the core shape. Magnetic and Mössbauer studies showed that the Curie temperature of synthesized CS $MgFe_2O_4/SiO_2$ MNCs is in the region of 320 K. CS nanospheres feature a narrow size distribution and are not agglomerated, which promotes weakening the interaction between particles. Thus, the use of oxygen catalyst makes it possible to form a biocompatible silica layer on the surface of $MgFe_2O_4$ magnetic nanospheres by the sol–gel method, and to produce CS $MgFe_2O_4/SiO_2$ MNCs promising for biomedical applications as heat sources in magnetically induced hyperthermal therapy.

REFERENCES

1. K. Hayashi, Y. Sato, W. Sakamoto, and T. Yogo, ACS Biomater. Sci. Eng. **3**, 95 (2017).
2. D. Ortega and Q. Pankhurst, in *Nanoscience. Nanostructures Through Chemistry* (R. Soc. Chem., Cambridge, 2013), Vol. 1, p. 60.
3. Z. Ling-Yun, L. Jia-Yi, O. Wei-Wei, L. Dan-Ye, L. Li, L. Li-Ya, and T. Jin-Tian, Chin. Phys. B **22**, 108104 (2013).

4. P. Guardia, A. Riedinger, H. Kakwere, F. Gazeau, and T. Pellegrino, in *Bio- and Bioinspired Nanomaterials*, Ed. by D. Ruiz-Molina, F. Novio, and C. Roscini (Wiley-VCH, Weinheim, 2015), Part 6.
5. I. Sharifi, H. Shokrollahi, and S. Amiri, J. Magn. Magn. Mater. **324**, 903 (2012).
6. H. Aono, T. Naohara, T. Maehara, H. Hirazawa, and Y. Watanabe, J. Ceram. Soc. Jpn. **122**, 237 (2014).
7. M. R. Barati, C. Selomulya, and K. Suzuki, J. Appl. Phys. **115**, 17B522 (2014).
8. M. A. Amer, T. Meaz, S. Attalah, and F. Fakhry, J. Magn. Magn. Mater. **401**, 150 (2016).
9. B. Antic, N. Jovic, M. B. Pavlovic, A. Kremenovic, D. Manojlovic, M. V. Vasic, and A. S. Nikolic, J. Appl. Phys. **107**, 043525 (2010).
10. H. Das, N. Sakamoto, H. Aono, K. Shinozaki, H. Suzuki, and N. Wakiya, J. Magn. Magn. Mater. **392**, 91 (2015).
11. H. Das, N. Debnath, A. Toda, T. Kawaguchi, N. Sakamoto, H. Aono, K. Shinozaki, H. Suzuki, and N. Wakiya, Adv. Powder Technol. **28**, 1696 (2017).
12. V. Šepelák, Ann. Chim. Sci. Mater. **27**, 61 (2002).
13. G. H. An, T. Y. Hwang, J. Kim, J. Kim, N. Kang, S. Kim, Y. M. Choi, and Y. H. Choa, J. Alloys Compd. **583**, 145 (2014).
14. H. S. Kang, Y. C. Jang, H. Y. Koo, S. H. Ju, D. Y. Kim, S. K. Hong, J. R. Sohn, K. Y. Jung, and S. B. Park, Mater. Sci. Eng. B **127**, 99 (2006).
15. M. Eslamian, M. Ahmed, and N. Ashgriz, Nanotechnology **17**, 1674 (2006).
16. M. Coskun and M. Korkmaz, J. Nanopart. Res. **16**, 2316 (2014).
17. B. Sahoo, K. S. P. Devi, S. Dutta, T. K. Maiti, P. Pramanik, and D. Dhara, J. Colloid Int. Sci. **431**, 31 (2014).
18. S. Kralj, D. Makove, S. Campelj, and M. Drofenik, J. Magn. Magn. Mater. **322**, 1847 (2010).
19. Y. G. Toropova, A. S. Golovkin, A. B. Malashicheva, D. V. Korolev, A. N. Gorshkov, K. G. Gareev, M. V. Afonin, and M. M. Galagudza, Int. J. Nanomed. **12**, 593 (2017).
20. R. G. Digigow, J. F. Dechezelles, H. Dietsch, I. Geissbuhler, D. van Cheke, C. Geers, A. M. Hirt, B. R. Rutishauser, and A. P. Fink, J. Magn. Magn. Mater. **362**, 72 (2014).
21. M. E. Khosroshahi and L. Ghazanfari, Mater. Sci. Eng. C **32**, 1043 (2012).
22. O. Kesmez, E. Burunkaya, N. Kiraz, H. E. Camurlu, M. Asilturk, and E. Arpac, J. Non-Cryst. Solids **357**, 3130 (2011).
23. T. K. H. Ta, M.-T. Trinh, N. V. Long, T. T. M. Nguyen, T. L. T. Nguyen, T. L. Thuoc, B. T. Phan, D. Mott, S. Maenosono, H. Tran-Van, and V. H. Le, Colloids Surf. A **504**, 1 (2016).
24. J. Hua, Y. Liu, L. Wang, M. Feng, J. Zhao, and H. Li, J. Magn. Magn. Mater. **402**, 166 (2016).
25. A. Kaide and T. Saeki, Avd. Powder Technol. **25**, 773 (2014).
26. L. P. Singh, S. K. Bhattacharyya, R. Kumar, G. Mishra, U. Sharma, G. Singh, and S. Ahalawat, Adv. Colloid Interface Sci. **214**, 17 (2014).
27. N. Wakiya, M. Yamasaki, T. Adachi, A. Inukai, N. Sakamoto, D. Fu, O. Sakurai, K. Shinozaki, and H. Suzuki, Mater. Sci. Eng. B **173**, 195 (2010).
28. M. E. Matsnev and V. S. Rusakov, AIP Conf. Proc. **1489**, 178 (2012).
29. M. Abbas, B. P. Rao, M. N. Islam, S. M. Naga, M. Takahashi, and C. Kim, Ceram. Int. **40**, 1379 (2014).
30. R. Ullah, B. K. Deb, and M. Y. A. Mollah, Int. J. Comps. Mater. **4**, 135 (2014).
31. W. Fu, H. Yang, Q. Yu, J. Xu, X. Pang, and G. Zou, Mater. Lett. **61**, 2187 (2007).
32. M. R. Barati, C. Selomulya, and K. Suzuki, J. Appl. Phys. **115**, 17B522-3 (2014).
33. M. A. Chuev, V. M. Cherepanov, and M. A. Polikarpov, JETP Lett. **92**, 21 (2010).
34. D. H. Jones and K. K. P. Srivastava, Phys. Rev. B **34**, 7542 (1986).
35. J. K. Srivastava and R. P. Sharma, Phys. Status Solidi **35**, 491 (1969).
36. S. Morup, J. A. Dumesic, and H. C. Topsoe, in *Applied Mössbauer Spectroscopy*, Ed. R. L. Cohen (Academic, New York, 1980), p. 28.
37. S. M. Patange. S. S. Desai, S. S. Meena, S. M. Yusuf, and S. E. Shirsath, RSC Adv. **5**, 91482 (2015).
38. K. Sharma, S. S. Meena, S. Saxena, S. M. Yusuf, A. Srinivasan, and G. P. Kothiyal, Mater. Chem. Phys. **133**, 144 (2012).
39. Y. L. Song, S. C. Tsai, C. Y. Chen, T. K. Tseng, C. S. Tsai, J. W. Chen, and Y. D. Yao, J. Am. Ceram. Soc. **87**, 1864 (2004).
40. A. M. Glezer and I. E. Permyakova, *Melt-Quenched Nanocrystals* (Fizmatlit, Moscow, 2012; CRC, Boca Raton, FL, 2013).

Translated by A. Kazantsev